Ductility improvement of Mg alloys by solid solution: Ab initio modeling, synthesis and mechanical properties

S. Sandlöbes [a], Z. Pei [a,b], M. Friák [a,b,c,*], L.-F. Zhu [a], F. Wang [a], S. Zaefferer [a], D. Raabe [a], J. Neugebauer [a]

[a] *Max-Planck-Institut für Eisenforschung GmbH, Max-Planck-Str. 1, D-40237 Düsseldorf, Germany*
[b] *Aachen Institute for Advanced Study in Computational Engineering Science (AICES), RWTH Aachen University, Schinkelstraße 2, D-52062 Aachen, Germany*
[c] *Institute of Physics of Materials of the Academy of Sciences of the Czech Republic, v.v.i., Žižkova 22, 6161 62 Brno, Czech Republic*

Abstract

The I_1 intrinsic stacking fault energy (I_1 SFE) serves as an alloy design parameter for ductilizing Mg alloys. In view of this effect we have conducted quantum–mechanical calculations for $Mg_{15}X$ solid-solution crystals (X = Dy, Er, Gd, Ho, Lu, Sc, Tb, Tm, Nd, Pr, Be, Ti, Zr, Zn, Tc, Re, Co, Ru, Os, Tl). We find that Y, Sc and all studied lanthanides reduce the I_1 SFE and render hexagonal closed-packed (hcp) and double hcp phases thermodynamically, structurally and elastically similar. Synthesis, experimental testing and characterization of some of the predicted key alloys (Mg–3Ho, Mg–3Er, Mg–3Tb, Mg–3Dy) indeed confirm reduced I_1 SFEs and significantly improved room-temperature ductility by up to 4–5 times relative to pure Mg, a finding that is attributed to the higher activity of non-basal dislocation slip.
© 2014 Acta Materialia Inc. Published by Elsevier Ltd. All rights reserved.

1. Introduction

Magnesium-based alloys are attractive for structural applications owing to their low mass density, good castability and efficient recyclability [1,2]. However, wider application of sheet Mg is hindered by its poor room-temperature formability, which is caused by pronounced basal slip and a strong basal-type texture [3]. It was observed that alloying Y and/or certain rare earth (RE) elements such as Ce can have positive effects on structural Mg alloys. Among these effects are texture weakening (e.g.

[4–19], and an increase in room-temperature ductility (e.g. [4,5,19–25,11,26,27]).

Many phenomenological studies have been performed on the influence of RE addition on Mg texture formation [4–19]. While pure Mg and conventional Mg alloy sheets typically show a strong basal texture [5–7], Mg–RE alloys have a weaker basal-type texture which is characterized by the broadening of the basal poles towards the sheet rolling direction (RD), leading to the so-called r-type texture [5,8,9] or towards the transverse direction (e.g. [5]). Extrusion of Mg–RE alloys leads to the formation of a weak $\langle 1\,1-2\,1 \rangle$ fibre texture [9–11,19], which is also referred to as a RE texture component [6,12]. The texture weakening effect was attributed to grain boundary pinning at Mg–RE precipitates [11,13] and to local lattice rotations around the precipitates [14]. Additionally, it was shown that

---

recrystallization nuclei at local deformation bands in Mg–Y and Mg–RE alloys have more random orientations than those formed more remotely from local deformation bands [15,16]. Talal et al. [4] studied the role of RE addition on the texture and deformation behaviour of Mg alloys and concluded from their experimental results that deformation mechanisms other than just basal ⟨a⟩ slip and tensile twinning were most likely active. Other studies [17,21] reported more intense activity of compression/secondary twinning [17,21] and non-basal dislocation slip [21,22,24,25] in RE-containing alloys, when compared to conventional Mg alloys and the formation of homogeneously distributed deformation or shear bands [17,20,21,28].

None of these studies addressed the underlying RE-induced plasticity mechanisms which are, hence, not fully understood yet. More specifically, the origin of the beneficial Y and RE solid-solution effects on the ductilization of Mg remains unresolved.

Atomistic studies using density functional theory (DFT) and molecular dynamics (MD) calculations aiming at clarifying the influence of solutes on the mechanical response of Mg alloys have been performed for $b = [\bar{2}\,1\,1\,0]$ basal dislocations and basal I_2 stacking faults [29]. The DFT results were used as input parameters to the Fleischer solid-solution strengthening model [29–31]. These results suggest that solutes increasing the I_2 stacking fault energy (SFE) lead to improved cross-slip probability of basal dislocations onto prismatic planes and, thus, improve ductility [29]. Chen and Boyle [32] performed ab initio calculations of the elastic moduli and electronic bonding character of binary Mg–Al, Mg–Zn and Mg–Y (7.143 at.%) to evaluate solid-solution strengthening. Using the Cauchy pressures as an indicator of the bonding character, the Mg–Y alloy revealed the highest bond strengths in this study [32]. It was suggested that Y enhances the brittleness of Mg, which contradicts the experimental observations. In conclusion, no explanation for the RE/Y ductilization was identified.

In a previous study we reported that single-phase solid-solution Mg–3 wt.% Y alloys show an increase in room-temperature ductility by about 5 times compared to pure Mg, while maintaining a comparable strength and work hardening [21]. Through transmission electron microscopy (TEM) combined with scanning electron microscopy electron backscatter diffraction (SEM-EBSD) slip trace analysis of active dislocations [51] it was shown that the ductility increase is related to higher activities of non-basal dislocation slip providing a ⟨c⟩-deformation component in Mg–Y. Using combined TEM and ab initio methods, this enhanced activity of ⟨c + a⟩ dislocations was correlated with a decreased I_1 intrinsic stacking fault energy (SFE) (sessile intrinsic stacking fault; ABABACAC stacking) [33].

The identification and quantification of the key parameter I_1 SFE as a pathway towards the design of ductile Mg solid-solution alloys thus provides a systematic approach to identify further favourable alloying elements. In this study we use and evaluate the parameter I_1 SFE of Mg–X solid-solution alloys as a basis for a theory-guided alloy design approach for creating more ductile Mg alloys. The predictions are compared to corresponding experiments on materials synthesized by liquid metallurgy and subsequent hot rolling.

2. Theoretical and experimental methods

2.1. Theoretical alloy design guideline and simulation procedure

Based on the observation that the chemical manipulation of the I_1 SFE through solid-solution alloying can serve as a guideline to ductilize Mg, we have chosen the following theoretical alloy design strategy: DFT calculations [34,35] were applied to determine the intrinsic stacking fault (ISF) energies using the axial next-nearest-neighbour Ising (ANNNI) model [36]. The ANNNI model represents an energetic approximation of the crystal containing the type of stacking faults studied here. The model employs energies of the defect-free bulk crystals in conjunction with different stacking sequences along one of the crystallographic axes of the lattice. The approach has been successfully applied to study stacking faults, e.g. in austenitic stainless steels [37], Fe–Mn alloys [38] and Mg–Y alloys [33].

The ISF energy is defined as the energy difference among crystals with and without an ISF defect, E_{ISF} and E_0, respectively, divided by the ISF area A:

$$\gamma^{ISF} = \frac{E^{ISF} - E_0}{A} \qquad (1)$$

Within the ANNNI model [37], both energies are expanded into series:

$$E = -\sum_n \sum_i J_n S_i S_{i+n} \qquad (2)$$

with the atomic layers i and $i + n$, characterized by the corresponding generalized spin-numbers S_i and S_{i+n}, interacting via the interaction parameters J_n. For a hexagonal close-packed (hcp) lattice, truncating the series after the second expansion term (the second-order ANNNI approximation), the following expression for the I_1 SFE (local double hcp (dhcp) stacking), is obtained:

$$E_{SF1} - E_0 \approx 4J_2 - 2J_1 = 2(E_{dhcp} - E_{hcp}) \qquad (3)$$

In this equation E_{SF1} is the I_1 SFE, E_0 is the energy of the defect-free hcp crystal, E_{hcp}, and E_{dhcp} are the total energies of hcp (...ABAB... stacking) and dhcp (double hcp: ...ABAC... stacking of the intrinsic I_1 stacking faults), respectively. Consequently, the I_1 SFE depends only on the energy difference between the hcp and dhcp stacking sequences (both with the hcp equilibrium volume) of Mg–Y crystals (for further details see Ref. [33]).

The ab initio calculations of I_1 SFEs were performed for a set of Mg–X alloys with solutes X crystallizing in a

hexagonal structure including both lanthanides (X = Dy, Er, Gd, Ho, Lu, Tb, Tm, Nd, Pr) and non-lanthanides (X = Sc, Be, Ti, Zr, Zn, Tc, Re, Co, Ru, Os, Tl). Radioactive elements were excluded. Also, the selection was limited to those elements for which a reliable (i.e. ground state correctly predicting) projector augmented wave (PAW) potential exists in the Vienna Ab initio Simulation Package (VASP) database. An impact of other solutes with non-hexagonal structures on the materials properties of Mg alloys is a topic of our future research.

In this work all DFT calculations were performed using VASP [39–41] in conjunction with the PAW basis set [41] and the Perdew–Burke–Ernzerhof (PBE) exchange–correlation functional [42]. The I_1 ISF energies were calculated (i) for pure Mg employing four-atom cells with a $36 \times 36 \times 12$ Monkhorst–Pack **k**-point mesh, and (ii) for Mg alloys containing 6.25 at.% selected solute atoms, i.e. the stoichiometry $Mg_{15}X$ (X = Dy, Er, Gd, Ho, Lu, Sc, Tb, Tm, Nd, Pr, Be, Ti, Zr, Zn, Tc, Re, Co, Ru, Os, Tl). It should be noted that the stacking fault geometry is modeled within the ANNNI model only indirectly, employing the energetics of different (hcp and dhcp) stacking sequences of hexagonal (0001) planes (see details in our previous work [33]). Therefore, a layer-resolved local concentration of solutes exactly at the stacking fault cannot be defined, but our recent study of generalized stacking fault energies [43] showed that the impact of solutes on the energetics of stacking faults decreases with increasing distance from the plane of the fault. 16-atom $2 \times 2 \times 2$ hcp-based or $2 \times 2 \times 1$ dhcp-based supercells were used in the calculations. The corresponding Monkhorst–Pack **k**-point mesh was $10 \times 10 \times 16$ for supercells containing 16 atoms. The cut-off energy E_{cut} was set to 350 eV. The plane-wave basis set and the **k**-point meshes were carefully tested and ensured an error of less than 1 meV per atom when calculating stacking fault energies. Unless explicitly stated, internal coordinates of atoms within the supercells as well as the shape of the supercells were fully optimized.

2.2. Synthesis, processing, and experimental characterization

The alloys Mg–3 wt.% X (X = Ho, Er, Tb, Dy) were chosen as example materials to confront the ab initio predictions with corresponding mechanical data obtained on real materials. For this purpose, these alloys were melted and solidified in an induction furnace under Ar pressure (15 bar) in a steel crucible. Homogenization annealing to obtain single-phase (hcp) solid-solution alloys was performed at 500 °C for 10 h under Ar atmosphere. Alloys were then hot rolled at 450 °C from a thickness of 30 mm to 50% engineering thickness reduction with thickness reductions of 12–15% per pass. A recrystallization annealing was performed for 15 min at 400 °C to obtain 35–45 μm grain sizes and a basal-type crystallographic texture. Tensile and compression tests were performed on a Roell/Zwick universal testing machine at room temperature with an initial strain rate of $10^{-3}\,s^{-1}$. For compression tests,

cylinders with a diameter of 5.0 mm and a height of 10.0 mm were cut by spark erosion. Tensile samples with a width of 4 mm and a gauge length of 20 mm were prepared and tested according to DIN 50125. The extension direction was parallel to the former RD. Cold rolling of 15 mm thick sheets was performed on a laboratory rolling mill to a total thickness reduction of 40% with 8–10% thickness reduction steps per pass. Samples for microstructure characterization were taken after each 10% reduction step. SEM and SEM-EBSD were performed in a field-emission gun electron microscope (Zeiss XB1540, operated at 15 kV). The SEM-EBSD measurements were conducted on longitudinal RD–normal direction (ND) sections, and the samples were prepared by mechanical polishing followed by electrolytic polishing using AC2 soft solution (90 s at 30 V, −25 °C). TEM observations were performed on a CM20 microscope equipped with a LaB_6 filament at 200 kV. TEM specimens were prepared from longitudinal RD–ND sections. Discs 3 mm in diameter of were cut using spark erosion; these discs were mechanically ground to 130–150 μm thickness and then electropolished (Struers Tenupol) until perforation using a solution of 3 vol.% perchloric acid in ethanol (12.5 V, −30 °C).

3. Results

3.1. Theoretical results

The computed I_1 ISF energies for the different binary alloys are summarized in Table 1 and Fig. 1. In this study we have focused specifically on solutes crystallizing in the hcp structure but a corresponding study on other solutes is under way. We find that alloying reduces the I_1 ISF energies (relative to the value for pure Mg) only in case of the lanthanides and for Y and Sc. All other non-lanthanides increase the I_1 ISF energies compared with that of pure Mg (20–50 mJ m^{-2}).

Table 1
DFT computed values of the I_1 SFE in $Mg_{15}X$ crystals (X = Dy, Er, Gd, Ho, Lu, Sc, Tb, Tm, Nd, Pr, Y, Be, Ti, Zr, Zn, Tc, Re, Co, Ru, Os, Tl) and the computed values for pure Mg.

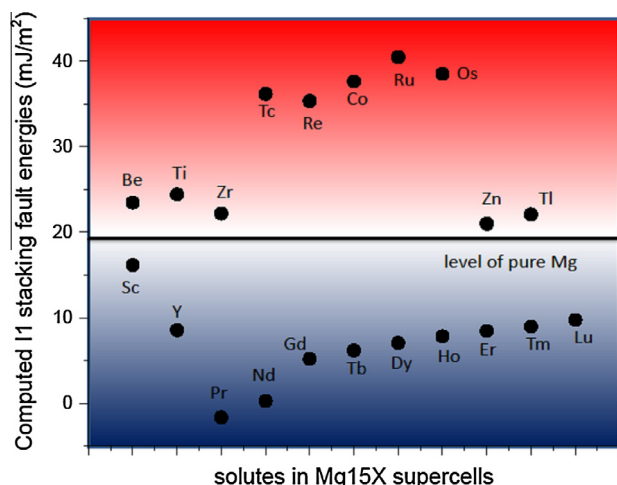| Element	Atomic no.	I_1 SFE (mJ m^{-2})	Element	Atomic no.	I_1 SFE (mJ m^{-2})
Sc	21	16.16	Be	4, IIA	23.48
Pr	59	−1.65	Ti	22, IVB	24.44
Nd	60	0.25	Zr	40, IVB	22.18
Gd	64	5.20	Tc	43, VIIB	36.19
Tb	65	6.17	Re	75, VIIB	35.35
Dy	66	7.06	Co	27, VIIIB	37.64
Ho	67	7.82	Ru	44, VIIIB	40.50
Er	68	8.45	Os	76, VIIIB	38.54
Tm	69	8.96	Zn	30, IIB	20.98
Lu	71	9.75	Tl	81, IIIA	22.09
Y	39	8.52			

Fig. 1. DFT computed values of the I_1 ISF energies in $Mg_{15}X$ crystals (X = Dy, Er, Gd, Ho, Lu, Sc, Tb, Tm, Nd, Pr, Y, Be, Ti, Zr, Zn, Tc, Re, Co, Ru, Os, Tl) with respect to the value for pure Mg.

3.2. Experimental results

The grain sizes and textures of the synthesized Mg–RE alloys were controlled to be similar and, hence, comparable to the results obtained on pure Mg and Mg–3Y in a previous study [22]. The recrystallized samples show a c-type texture without pole splitting and grain sizes of ~40 ± 5 μm.

The mechanical testing of these new alloys (solid-solution Mg–RE alloys with predicted reduced I_1 SFE; see Fig. 1) showed indeed significantly improved room-temperature ductilities. Fig. 2 illustrates the tensile and compressive stress–strain curves of the new alloys and of pure Mg for comparison. Cold rolling of the new samples was performed and total thickness reductions of more than 40% were obtained with steps of 8–10% reduction per pass; the initial sheet thickness amounted to 15 mm. Fig. 3 shows the macrostructure of the new alloys after each cold-rolling pass. The images reveal that these new Mg–RE alloys could

be cold rolled very well (using rather severe reductions per pass) without forming any side cracks. In comparison, pure Mg has already completely fractured along macroscopic shear bands after as little as 20% cold rolling (Fig. 3a).

The deformation microstructures and crystallographic textures were measured after each 10% thickness reduction pass using SEM-EBSD. The corresponding SEM-EBSD analyses are given in Fig. 4 in terms of inverse pole figure (IPF) and nearest-neighbour kernel average misorientation (KAM) maps. KAM maps are used in the microstructure analysis as a measure of the dislocation density, which quantifies the local lattice curvature and is retrieved directly from the EBSD maps.

The deformation microstructures of the new alloys are characterized by a homogeneous strain distribution with small and localized deformation bands homogeneously distributed in the microstructure. These deformation bands are visible in the KAM maps as regions of higher misorientation in Fig. 4; they are formed either within single grains or at the boundary of two grains. With increasing rolling deformation the number and misorientation of these local deformation bands as well as the average in-grain misorientation patterning is increasing.

Similar deformation microstructures were observed in the ductile Mg–3Y alloy [21]. In contrast, pure Mg deforms via strain localization and early cracking along these localized regions (macro shear bands) [21].

Compared to the very intense shear banding observed in pure Mg [21], the deformation microstructure in the presently synthesized Mg–RE alloys is characterized by a high deformation band density as well as smaller local misorientation and smaller local strains associated with each band. This leads to an altogether more homogeneous deformation microstructure of the new materials. Deformation bands do not become critical enough to cause early failure when the material is cold formed.

Observation and identification of dislocations on 4% deformed (cold rolled, i.e. compression) material was
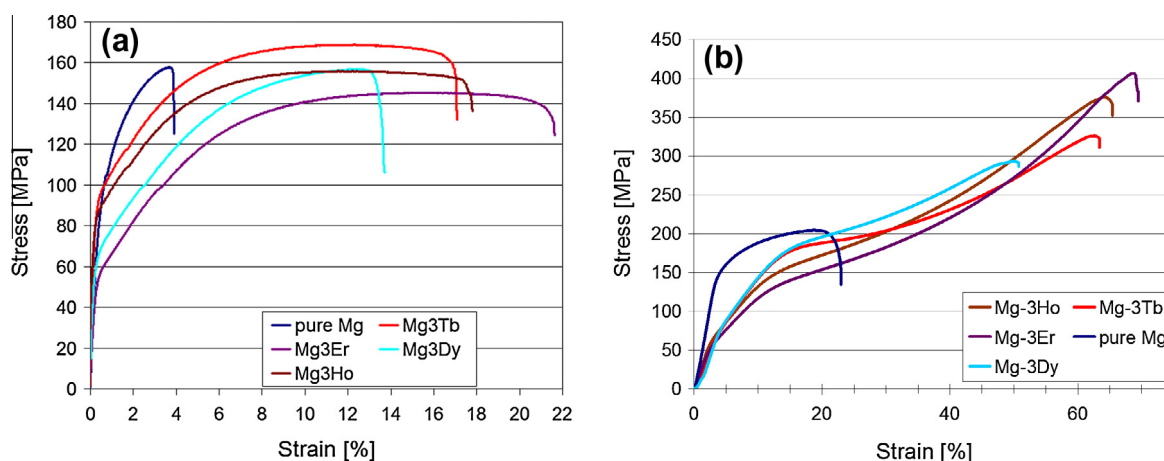

Fig. 2. Tensile (a) and compressive (b) stress–strain curves of the new Mg–3RE (RE = Er, Dy, Tb, Ho) alloys and pure Mg; the initial strain rate amounted 10^{-3} s^{-1}.
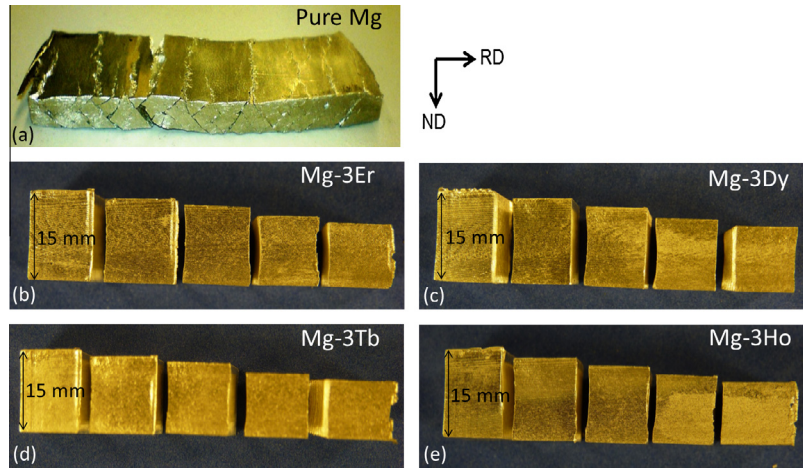
Fig. 3. Optical photographs of (a) 20% cold-rolled pure Mg and (b)–(e) cold-rolled Mg–3RE (RE = Er, Dy, Tb, Ho) after each 10% thickness reduction; the new Mg–RE alloys could be very easily cold rolled without forming any side cracks; pure Mg has already completely fractured along macroscopic shear bands after 20% cold rolling.
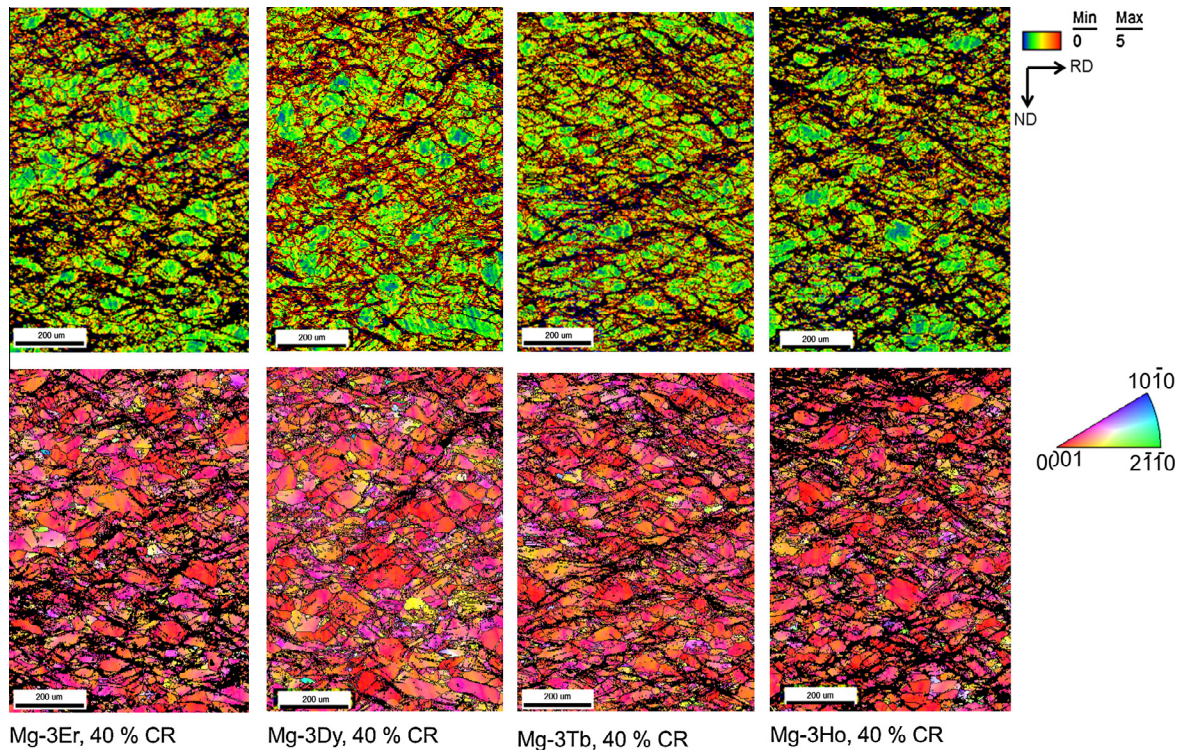

Fig. 4. Inverse pole figure (IPF) and kernel average misorientation (KAM) maps of cold-rolled microstructures of Mg–3RE (RE = Er, Dy, Tb, Ho) after 40% cold rolling; the deformation microstructures are characterized by a homogeneous strain distribution with small and local deformation bands homogeneously distributed in the microstructure.

performed applying the $g \cdot b = 0$ (where g is the diffraction vector) criterion in the TEM. For each alloy dislocation observation in several two-beam conditions, $g = 0002$, $g = hki0$ ($g = 11-20$ or $g = -2110$) and $g = hkil$ ($g = 11-22$, $g = 1-21-2$ or $g = 10-11$), was performed. According to the $g \cdot b = 0$ criterion dislocations with a $\langle c \rangle$ component are visible under $g = 0002$ and $g = hkil$ and invisible under $g = hki0$, while dislocations with an $\langle a \rangle$ component are visible under $g = hki0$ and $g = hkil$ and

invisible under $g = 0002$. Fig. 5 shows TEM dark-field images of $g = 0002$ and $g = hki0$ ($g = 11-20$ and $g = -2110$) two-beam conditions of the new alloys, respectively. As described above, all dislocations which are visible in both micrographs have both $\langle a \rangle$ and $\langle c \rangle$ components. It is evident from the micrographs that in all new alloys, as well as basal $\langle a \rangle$ dislocations, pyramidal $\langle c + a \rangle$ dislocations are observed. Additionally, prismatic $\langle a \rangle$ dislocations were found in Mg–3Dy and Mg–3Ho.
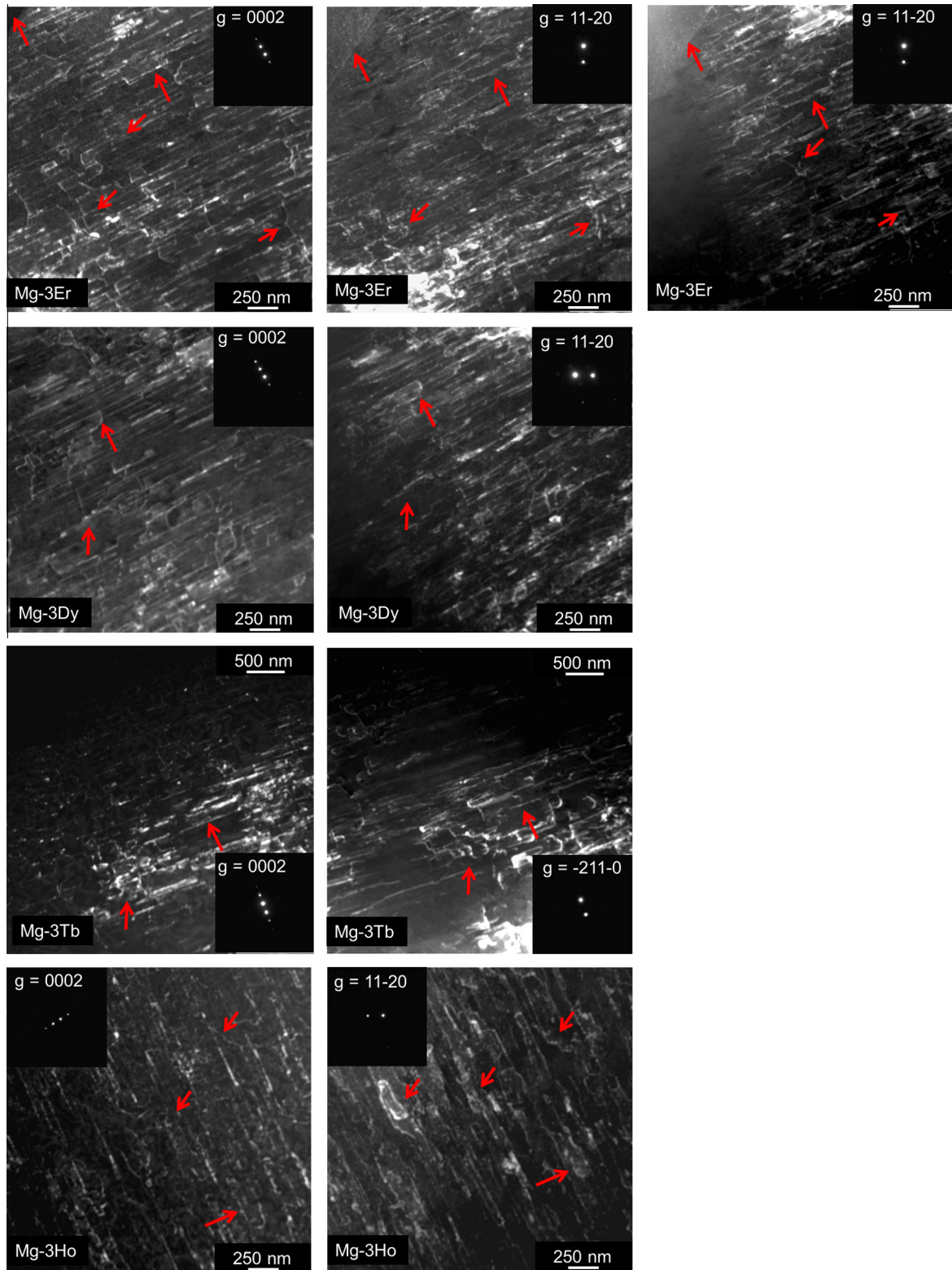
Fig. 5. TEM dark-field images of dislocations in 4% cold-rolled Mg–3RE (RE = Er, Dy, Tb, Ho); for the identification of the type of dislocations two different two-beam conditions, $g = 0002$, $g = \mathrm{x\,x\,x\,0}$ ($g = 11\,-20$ or $g = -2110$), are shown here; the analysis reveals a substantial number of pyramidal dislocations. For each alloy the same area is shown under different two-beam conditions; for orientation, red arrows are shown pointing to the same positions in the micrographs. (For interpretation of the references to colour in this figure legend, the reader is referred to the web version of this article.)
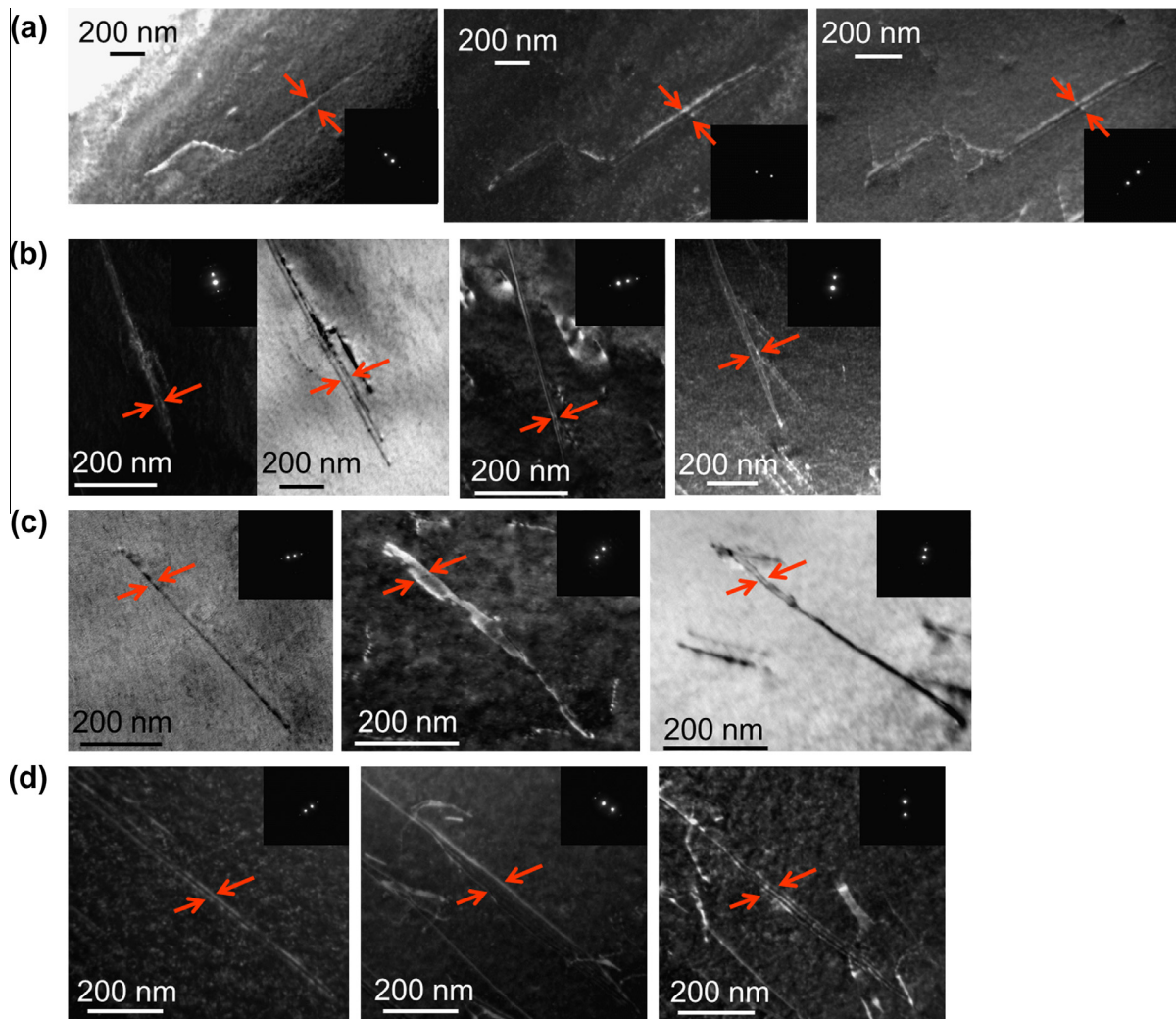
Fig. 6. TEM micrographs of I$_1$ ISFs in slightly (1%) cold-deformed Mg–3RE (RE = Er (b), Dy (c), Tb (d), Ho (a)). For each alloy the same area is shown under different two-beam conditions.

Additionally, a higher (compared to pure Mg) density of I$_1$ ISFs was observed in recrystallized and then slightly (∼1%) deformed specimens of the alloys Mg–3Er, Mg–3Tb, Mg–3Ho and Mg–3Dy. Burgers vector (**b**) analysis according to the **g** · **b** criterion of the bounding partial dislocations was performed. Selected TEM micrographs of I$_1$ stacking faults are presented in Fig. 6 for the Mg–RE alloys. From the observed high (compared to pure Mg) density and widths of the observed I$_1$ stacking faults, it is clear that the I$_1$ ISF energies are reduced compared to pure Mg in all four alloys studied.

4. Discussion

In this work we aim at achieving a better understanding of the origins of the ductilization effect of a set of Mg alloys from an atomistic and electronic standpoint and we limit ourselves to Mg solid solutions blended with a set of 21 elements that crystallize in hcp structures. A subsequent study of other solutes that do not crystallizing in hcp structures

will follow. A representative subset of these ab initio predicted materials was actually synthesized, processed, and mechanically and microstructurally characterized. The respective alloying elements where selected based on two criteria: (i) the I$_1$ SFE is expected to be decreased by alloying; (ii) the alloying element should have relatively high (>1 at.%) solid solubility in Mg.

A number of preceding studies have addressed the ductilization and softening effects associated with crystallographic textures, primary static and dynamic recrystallization, solid solution and precipitation strengthening and deformation characteristics of Y and/or RE alloying on Mg alloys [4–29]. Nevertheless, a more fundamental understanding of the atomic-scale interaction of Y and RE elements with the Mg matrix and the resulting effects on the macroscopic properties remains incomplete. Moreover, it is not clear why Y and lanthanides have very similar effects on the macroscopic mechanical behaviour of Mg when rendered into solid-solution alloys. Based on their electronic structure (within the lanthanide series the

4f electronic orbital is filled ($n − 2$ elements)) the lanthanides are known to have special properties, both in elemental form and as alloying elements in many systems [44,45]. This is, however, not the case for Y and Sc: both elements are $n − 1$ transition metals having no 4f electrons. This means that a clear common electronic property spectrum of Y and Sc on the one hand and the RE elements on the other hand, which influence so drastically the bulk properties of Mg towards an enhanced macroscopic ductility, has not been identified so far.

In a previous study, we showed by a combination of TEM measurements and ab initio calculations that the ductility increase in Mg–Y alloys is caused by an increased activity of $\langle c + a \rangle$ dislocation slip [21]. This facilitated activation of out-of-basal-plane shear modes through the addition of Y to Mg is correlated to a significantly decreased I_1 SFE [33]. Here, the I_1 SFE is decreasing with increasing Y concentration. In line with previous work on this problem [33] we propose that this reduction of the I_1 SFE can be used as a guiding parameter (among others) connected with the ductility increase in the Mg–Y system acting as follows: the enhanced ductility is caused by a high activity of pyramidal $\langle c + a \rangle$ dislocations as slip modes out of the basal plane. The nucleation of $\langle c + a \rangle$ dislocations is the critical step in providing out-of-basal-plane shear. This is associated with I_1 stacking faults: the sessile I_1 stacking faults, whose energy decreases with Y alloying, is bound by pyramidal partial dislocation. This dislocation arrangement enables the formation of dislocation structures on pyramidal planes. In line with the nucleation source configuration studied by Yoo et al. [46] we suggest that I_1 stacking faults act as heterogeneous nucleation sources for pyramidal $\langle c + a \rangle$ dislocations. Consequently, following our proposal, the observed (TEM) and calculated (DFT) reduced I_1 SFE through the addition of Y could cause the formation of stable I_1 stacking faults in Mg–Y alloys, and hence provide sources for $\langle c + a \rangle$ dislocations. The reduced SFE leads then to a higher probability of formation of SFI_1 nucleation sources and therefore higher ductility.

Therefore, we now used the I_1 SFE of Mg–X solid solutions more systematically as a guiding parameter for the design of a general class of ductile Mg alloys. An important aspect of this ab initio driven alloy design strategy is the opportunity to connect a macroscopic material property such as ductility and the underlying dislocation substructure directly with an atomic-scale quantity such as the I_1 stacking fault which is accessible to quantum mechanical predictions [33,47–50]. Based on ab initio predictions of these I_1 ISF energies, promising alloys, i.e. those characterized by a reduced I_1 SFE, were produced, homogenized, rolled, mechanically tested and characterized in terms of their microstructure, deformation mechanisms and I_1 SFE. In this study we experimentally confirm that alloys with theoretically predicted decreased I_1 SFE indeed possess significantly enhanced room-temperature ductility and experimentally observed decreased I_1 ISF energies.

4.1. Effects of structural, energetic, and elastic contributions to the I_1 SFE

The current predictions (Fig. 1, Table 1) show decreasing I_1 ISF energies for $Mg_{15}X$ where the solutes X are Y, Sc and all the lanthanides considered in our theoretical study. The ANNNI model provides detailed insights into I_1 SFE and their alloy dependence: within the ANNNI model, the I_1 SFE is (for a given chemical composition) expressed as the energy difference between the ground state energy of the bulk dhcp structure and the bulk hcp structure (both at the equilibrium volume of the hcp structure). The I_1 SFE would be zero in the case that both phases are structurally (volume per atom, c/a ratio), elastically (bulk modulus) and energetically (minimum of the energy vs. volume curve) equal.

In the following we discuss the impact of different solutes on the main parameters that determine the I_1 SFE (thermodynamically, structurally, energetically) for both hcp and dhcp structures.

4.2. Mg–lanthanides, Mg–Y, Mg–Sc solid solutions

The predicted structural, elastic and thermodynamic parameters of hcp and dhcp structures as well as the respective differences of these parameters between the hcp and dhcp structures for Mg with solutes of the lanthanide series, Y and Sc are summarized in Table 2 and visualized in Fig. 7. As shown in Fig. 7a, all studied lanthanide solutes have the same effect of reducing the difference between the total energies of hcp and dhcp structures as the most elementary contribution to the reduction of the I_1 SFE. Fig. 7b clearly shows how strongly (~80%) the differences in the c/a ratios of hcp and dhcp structures are reduced in $Mg_{15}X$ compounds (e.g. $c/a = 1.584$ for hcp vs. $c/a = 1.590$ for dhcp in the case of Ho additions) with respect to pure Mg ($c/a = 1.645$ for hcp vs. $c/a = 1.589$ for dhcp). Also, the absolute values of the c/a ratio for both structure types, hcp and dhcp, are significantly reduced with respect to pure hcp Mg. The reduction is nearly identical for all studied lanthanides. The relative differences in the volume per atom (see Fig. 7c) of the two structures are significantly decreased for all studied lanthanide solutes with negative values for the early lanthanides. Most notably, the solutes Y, Tb, Dy, Ho, Er and Tm render the volume per atom of $Mg_{15}X$ crystals nearly identical in both hcp and dhcp structures.

The relative difference of the bulk moduli of hcp and dhcp structures (Fig. 7d) is reduced for all lanthanide solutes, Sc and Y (compared with the value predicted for pure Mg) with a minimum value for Gd and Tb.

Our theoretical study thus predicts and explains a significant reduction of the I_1 SFE (as the parameter linked to macroscopic ductility of Mg–Y alloys) in the case of Y, Sc and lanthanide additions in the form of solutes in Mg alloys. Within the presented ab initio calculations the origin of this reduction is revealed to be a complex interplay

Table 2
Ab initio calculated structural, elastic and thermodynamic parameters of hcp and dhcp phases of $Mg_{15}X$ crystals, where X = lanthanide, Sc and Y. Listed are total energy differences $E_{dhcp} - E_{hcp}$ (meV per ion) between $Mg_{15}X$ crystals with dhcp and hcp stackings; volumes per atom V ($Å^3$ per ion); bulk moduli B (GPa) for both hcp and dhcp crystals together with their relative ratios. Crystals of $Mg_{15}X$ are described by the c/a ratios of hcp structures (or half these values in the case of dhcp structures).

| Element	Mg	Sc	Pr	Nd	Gd	Tb	Dy	Ho	Er	Tm	Lu	Y
Atomic no.	12	21	59	60	64	65	66	67	68	69	71	39
$E_{dhcp} - E_{hcp}$ (meV per ion)	5.4	4.5	−0.5	0.1	1.5	1.8	2.0	2.2	2.4	2.5	2.8	2.4
V_{hcp} ($Å^3$ per ion)	22.88	22.99	24.14	24.05	23.77	23.71	23.66	23.61	23.56	23.52	23.44	23.71
V_{dhcp} ($Å^3$ per ion)	22.94	23.01	24.09	24.01	23.75	23.70	23.65	23.61	23.56	23.52	23.45	23.70
$(V_{dhcp} - V_{hcp})/V_{hcp}$ (%)	0.24	0.09	−0.22	−0.18	−0.07	−0.05	−0.03	−0.02	0.00	0.02	0.04	−0.05
B_{hcp} (GPa)	36.3	37.8	35.5	35.8	36.6	36.8	36.9	37.0	37.1	37.2	37.3	35.9
B_{dhcp} (GPa)	35.9	37.5	35.3	35.5	36.5	36.7	36.8	36.9	36.9	37.0	37.1	35.8
$(B_{dhcp} - B_{hcp})/B_{hcp}$ (%)	−1.04	−0.72	−0.55	−0.91	−0.30	−0.30	−0.39	−0.45	−0.52	−0.57	−0.51	−0.38
$(c/a)^{hcp}$	1.645	1.594	1.571	1.572	1.580	1.582	1.584	1.586	1.587	1.589	1.593	1.582
$1/2(c/a)^{dhcp}$	1.589	1.602	1.577	1.578	1.587	1.588	1.590	1.592	1.593	1.595	1.599	1.587
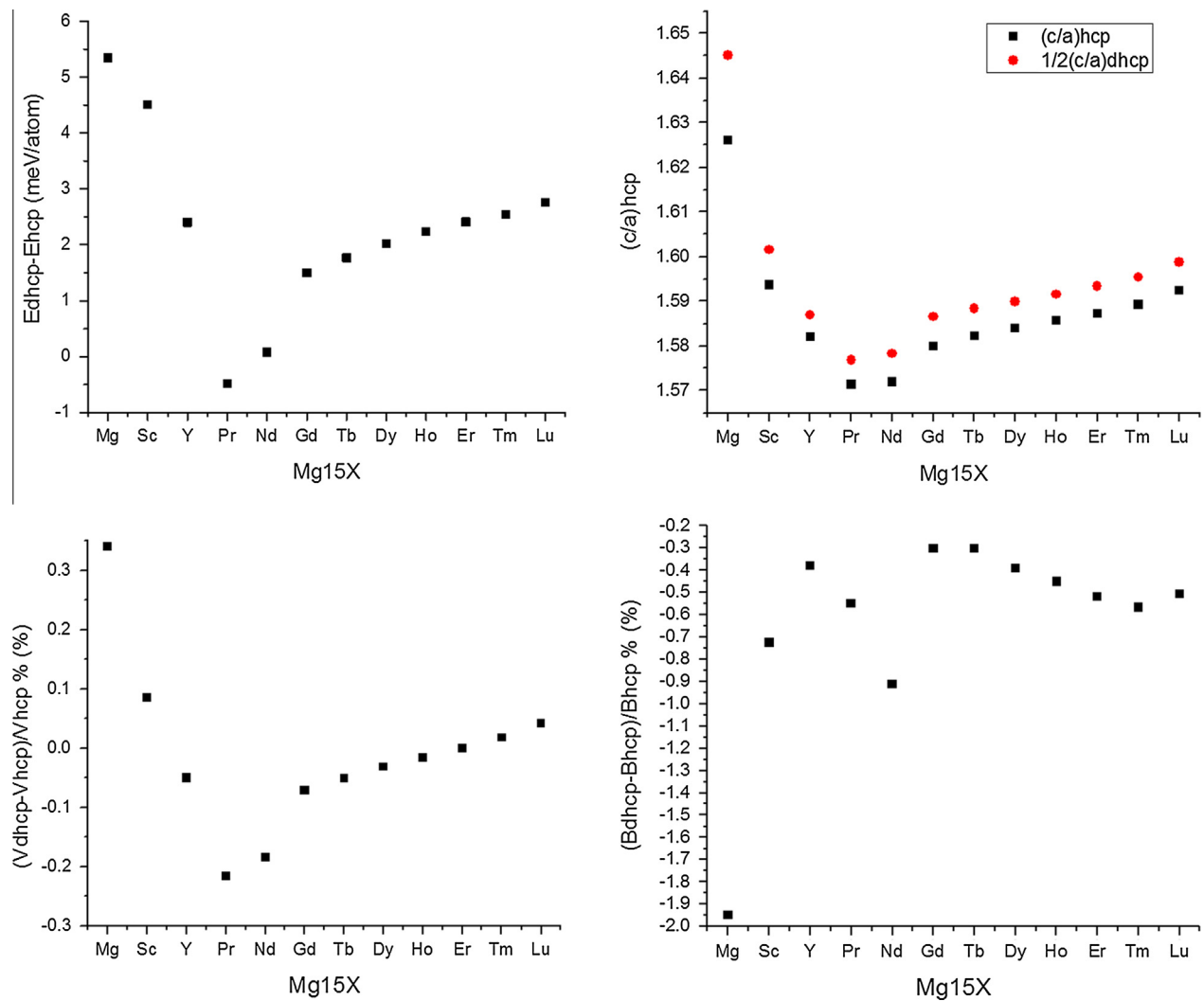
Fig. 7. Theoretically predicted differences of energetic, structural and elastic parameters of $Mg_{15}X$ crystals with X belonging to the lanthanide series (see also Table 2).

of these solutes acting in a number of manners on the internal materials characteristics, such as the volume per atom, the bulk modulus difference and the c/a ratio of hexagonal lattice parameters. Specifically, the values of these parameters in hcp and dhcp stackings become very similar, in fact nearly identical. This conclusion generalizes our findings

for Mg–Y alloys (for details, see Ref. [33]) to all Mg–RE alloys.

Besides the effects that these three parameters have directly on the change in the I_1 SFE, other more indirect interactions apply through the direct effects of solutes on dislocations and slip plane packing density. For instance, the volume change per atom acts on the dislocations through the size effect, which is in the analytical limit referred to as the parelastic effect; the change in bulk modulus is referred to as the dielastic effect, and the change in the c/a ratio affects the geometrical preference between basal slip, pyramidal and prism slip, and mechanical twinning. Hence, all these three parameters act simultaneously on the activation of non-basal slip leading to macroscopic ductilization. It is found that all the above-listed alloying elements (Y, Sc and lanthanides) that are reducing the I_1 SFE in fact also reduce the differences between the corresponding hcp and dhcp stacking heights regarding the studied thermodynamics, structural and elastic material parameters.

Based on these ab initio predictions four new representative alloys (Mg–3Tb, Mg–3Er, Mg–3Dy, Mg–3Ho) were metallurgically synthesized, mechanically tested and characterized. To reduce texture and grain size effects on the deformation behaviour the basal texturing and average grain sizes of the new alloys were controlled (see Section 3.2). Mechanical testing in tension (Fig. 2a) and compression (Fig. 2b) as well as cold rolling (Fig. 3) at room temperature clearly showed drastically improved room-temperature ductility of the new alloys under all these three boundary conditions. Microstructure characterization revealed homogeneous deformation and the activity of non-basal ($\langle c + a \rangle$) dislocations during deformation [21,51] in conjunction with reduced I_1 ISF energies. Thus, it was experimentally validated that the selected alloying elements (Er, Tb, Dy, Ho) significantly decrease the I_1 SFE as predicted via DFT and that this reduction in the I_1 SFE is accompanied by an increased activity of pyramidal $\langle c + a \rangle$ dislocation slip and improved room-temperature ductility.

4.3. Mg–non-lanthanides solid solutions

The calculated material parameters for non-lanthanide solutes are summarized in Table 3 and displayed in Fig. 8. It can be clearly seen that none of these solutes has an impact on the properties of $Mg_{15}X$ similar to that caused by Y, Sc and the lanthanides. Most notably, the total energy difference of the dhcp and hcp structures ($E_{dhcp} - E_{hcp}$ (meV per atom)) is not reduced for any of the non-lanthanide solutes studied here. Some of these solutes change one or more of these key characteristics similarly to the lanthanide solutes but none of them is predicted to change all of them. For example, $Mg_{15}Tc$ possesses nearly identical volume per atom for hcp and dhcp structures and a similar difference between the hcp and dhcp bulk moduli (though opposite sign), but the energy difference between hcp and dhcp structures of $Mg_{15}Tc$ is very high and the c/a ratios are only moderately reduced (when compared to the difference predicted for Mg). Zr and Tl alloying reduces some parameter differences and increases others. In the case of $Mg_{15}Tl$ the energy difference between hcp and dhcp structures is increased only weakly with respect to the corresponding value in Mg. The bulk moduli difference is reduced, the absolute values of the c/a ratios are comparable to each other, and the difference between the c/a ratios of dhcp and hcp structures is reduced in comparison to pure Mg. For $Mg_{15}Zr$ the energy difference ratio is only slightly increased and the volumetric difference is strongly reduced to nearly zero. The c/a ratios of $Mg_{15}Zr$ hcp and dhcp structures are reduced, but the bulk moduli difference ratio is increased.

Of the non-lanthanides with hexagonal structure studied here, only a few, namely Zn, Zr, Ti and Tl, are soluble in Mg or possess a low-melting eutectic with Mg. The room-temperature mechanical properties of three of these Mg alloy systems (that are predicted to increase the I_1 SFE) have been studied before, namely Mg–Ti, Mg–Zr and Mg–Zn [1,2,52–55,5,56–63]. Among these, Zr and Zn are very common alloying elements of commercial Mg alloys. Ai and Quan [52] tested the room-temperature

Table 3
Ab initio calculated structural, elastic and thermodynamic parameters of hcp and dhcp phases of $Mg_{15}X$ crystals, where X = non-lanthanide elements. Listed are total energy differences $E_{dhcp} - E_{hcp}$ (meV per ion) between $Mg_{15}X$ crystals with dhcp and hcp stackings, and volumes per atom V (Å^3 per ion) and bulk moduli B (GPa) for both hcp and dhcp crystals together with their relative ratios. Crystals of $Mg_{15}X$ are described by the c/a ratios of hcp structures (or half these values in the case of dhcp structures).

| Element	Mg	Be	Ti	Zr	Tc	Re	Co	Ru	Os	Zn	Tl
Atomic no. and group	12, IIA	4, IIA	22, IVB	40, IVB	43, VIIB	75, VIIB	27, VIIIB	44, VIIIB	76, VIIIB	30, IIB	81, IIIA
$E_{dhcp} - E_{hcp}$ (meV per ion)	5.4	6.2	6.7	6.2	9.6	9.3	10.0	10.8	10.2	5.7	6.1
V_{hcp} (Å^3 per ion)	22.85	21.87	22.29	22.73	21.39	21.33	21.46	21.31	21.13	22.26	23.04
V_{dhcp} (Å^3 per ion)	22.93	21.95	22.31	22.73	21.40	21.37	21.45	21.34	21.16	22.33	23.11
$(V_{dhcp} - V_{hcp})/V_{hcp}$ (%)	0.34	0.34	0.09	0.03	0.04	0.17	−0.05	0.16	0.13	0.31	0.30
B_{hcp} (GPa)	36.3	37.0	40.6	39.6	42.5	43.3	38.5	42.9	43.8	36.8	35.6
B_{dhcp} (GPa)	35.6	36.7	40.3	39.3	42.1	42.8	38.4	42.4	43.4	36.5	35.4
$(B_{dhcp} - B_{hcp})/B_{hcp}$ (%)	−1.95	−0.84	−0.87	−0.89	−0.95	−1.18	−0.26	−1.18	−0.93	−0.87	−0.55
$(c/a)^{hcp}$	1.626	1.634	1.592	1.588	1.598	1.608	1.597	1.589	1.598	1.650	1.640
$1/2(c/a)^{dhcp}$	1.645	1.636	1.604	1.597	1.616	1.625	1.609	1.609	1.618	1.648	1.648
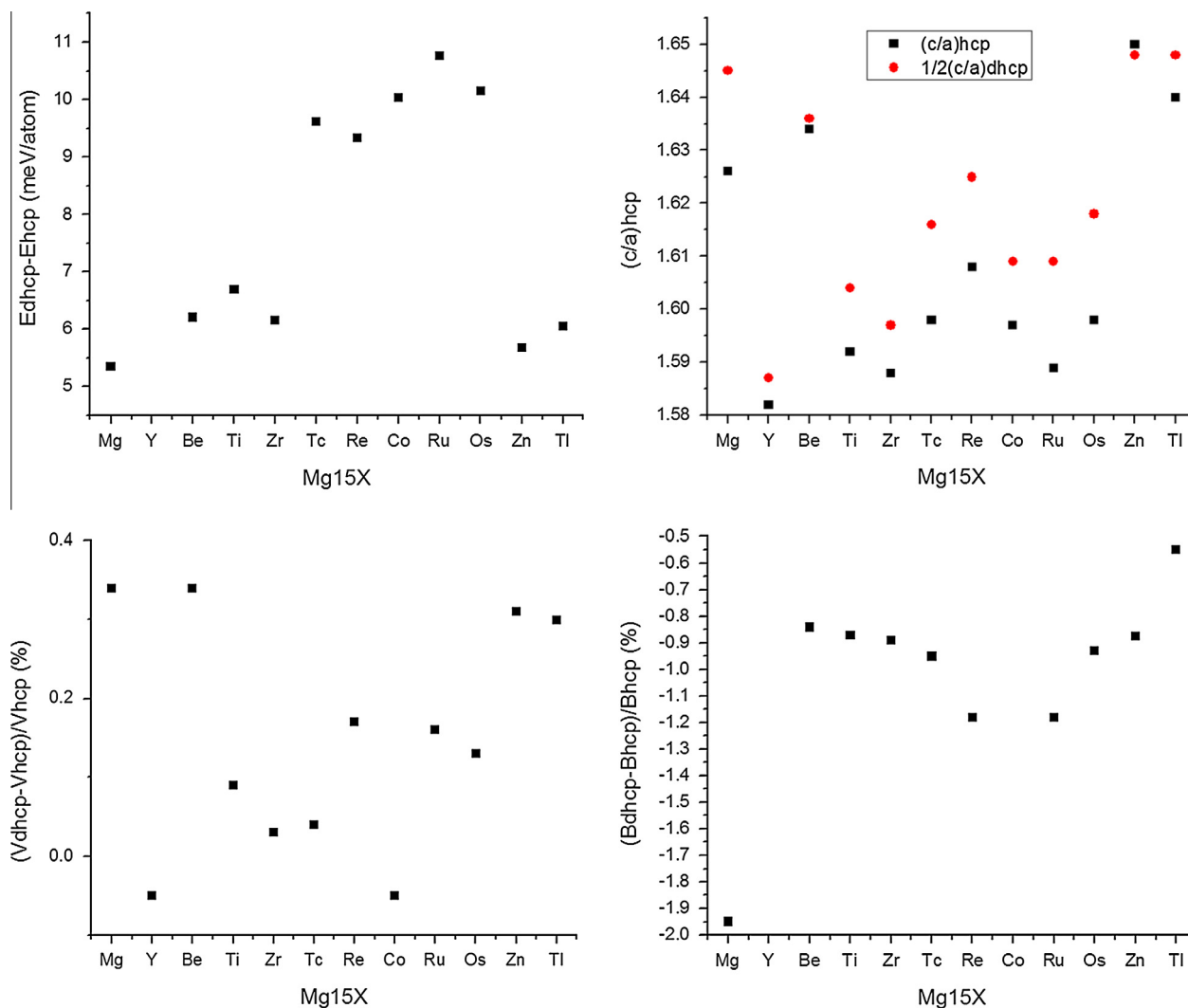
Fig. 8. Theoretically predicted differences of energetic, structural and elastic parameters of $Mg_{15}X$ crystals with hcp and dhcp stacking sequences with X being non-lanthanide atoms (see also Table 3).

mechanical properties of Mg alloyed with Ti in solid solution (powder metallurgical synthesis). They observed an increase in the strength and at the same time a drop in room temperature ductility through solid-solution alloying of Ti. Zr is widely used as a grain-refining alloying element in Mg alloys leading to an increase in strength but not in ductility, but it should be mentioned that the solubility of Zr is very low and the main effect of Zr on Mg lies in its grain refinement effect obtained via grain boundary pinning [2,53,56]. Zn is one of the most common alloying elements in commercial Mg alloys. Many effects are attributed to it, such as precipitation strengthening when alloyed together with Al, (e.g. [2,54]), hardening of the basal slip and softening of the prismatic slip [57,58] and grain refining [2,54,59–61]. Zn is known to cause a moderate increase in ductility, yet it does not cause such a substantial improvement in room-temperature ductility as observed for RE (e.g. [2,62–64]). Studies on the slip systems active during room-temperature deformation showed that only in

prismatically oriented grains non-basal dislocations (both prismatic $\langle a \rangle$ and pyramidal $\langle c + a \rangle$) are observed (e.g. [55,62]). The other orientations were found to deform mainly by twinning and basal dislocation slip during room-temperature deformation [55,62,63].

4.4. Main solid-solution effects on the ductilization of Mg alloys

The classical solid-solution strengthening and hardening models are based on the direct effects of the solute atom on dislocations either via interaction of the stress field induced by solute atoms with dislocations (solid solution strengthening) or via decreasing the energy barrier for cross-slip of dislocations (solid solution softening) [30,31,64]. In the present study a more indirect solid-solution effect is investigated, namely solid-solution alloying causing a reduction of the I_1 SFE and, hence, facilitating the formation of I_1 stacking faults. These I_1 stacking faults are supposed to

act as nucleation source for non-basal dislocations at room temperature.

Our analysis of the parameters determining the I_1 SFE reveals that there is not one single explicit parameter that exclusively controls this energy, but the effect is rather due to the combination of thermodynamic, structural and energetic (elastic energy) contributions. Here, we hypothesize that the thermodynamic contribution is represented by the energy difference between the dhcp and hcp structures having their respective equilibrium volumes. Structurally, energetically costly elastic strains would be induced in case of significant structural mismatch between the hcp and the dhcp phases. It is therefore advantageous if the dhcp stacking (I_1 stacking faults) has a similar volume per atom and a similar c/a lattice parameter ratio as the hcp Mg matrix. The bulk modulus determines how steeply the energy difference increases in the case of non-zero volumetric difference between the hcp and dhcp structures. A lower value of this elastic parameter for dhcp stacking therefore contributes to decreasing the I_1 SFE.

The fundamental atomistic parameters associated with these structural, thermodynamic and energetic parts of the I_1 SFE in solid-solution systems are related to (i) the atomic radius, (ii) the electronegativity and (iii) the bulk modulus difference of Mg and the solutes. Here, the atomic radius determines the contributions of structure, electronegativity (both structural and thermodynamic), and bulk modulus to the (elastic) energetic component of the I_1 SFE. Analysis of these parameters shows that all elements (lanthanides, Y, Sc) which reduce the I_1 SFE in Mg have (i) large atomic radii of $\geqslant 184$ pm (Mg: 145 pm), (ii) electronegativity values close to that of Mg (1.1–1.3) and (iii) bulk moduli close to Mg (32–56 GPa). A more detailed analysis of these parameters shows that Sc, which only moderately reduces the I_1 SFE of Mg fulfils all three criteria but its values are a bit away from those of Y and the lanthanides. It is revealed that none of the other elements (except lanthanides, Y and Sc) fulfils all three criteria.

5. Conclusions

We applied ab initio calculations to predict the I_1 SFE of various MgX solid-solution alloys. The I_1 SFE is proposed to be a suitable alloy design parameter to improve the ductility of Mg alloys. Here sessile I_1 stacking faults are proposed to act as continuous nucleation sources for $\langle c + a \rangle$ dislocations [33]. Following the ab initio predictions we produced and tested four new ductile binary Mg–RE alloys.

From our complementary theoretical and experimental study we conclude:

(i) The I_1 SFE and all thermodynamic, structural, and elastic differences contributing to the value of this energy are reduced for lanthanides and Y and Sc. The dhcp structure (i.e. the structure of the I_1 stacking faults) is effectively thermodynamically destabilized

with respect to the hcp phase, and it is thus made structurally and elastically better matching the hcp matrix surrounding the stacking fault.
(ii) Experimental testing and microstructural characterization of four new alloys (Mg–3Er, Mg–3Tb, Mg–3Dy, Mg–3Ho) with predicted decreased I_1 SFE was performed. All four alloys showed a significantly increased room-temperature ductility, an increased activity of non-basal (in particular $\langle c + a \rangle$ dislocations) dislocation slip and an experimentally observed decreased I_1 SFE.
(iii) All studied non-lanthanides excluding Y and Sc were predicted to increase the I_1 SFE.

In conclusion, we demonstrate that combining mechanism-oriented ab initio modeling with advanced experimental characterization methods facilitates the identification and understanding of critical microstructure parameters as a basis for advanced materials design of complex structural engineering materials.

Acknowledgments

References

[1] Mordike BL, Ebert T. Mater Sci Eng A 2001;302:37.
[2] Yang Z, Li JP, Zhang JX, Lorimer GW, Robson J. Acta Metall Sin (Engl Lett) 2008;21:313.
[3] Agnew SR, Horton JA, Yoo MH. Metall Mater Trans A 2002;33:851.
[4] Al-Samman T, Li X. Mater Sci Eng A 2011;528:3809.
[5] Bohlen J, Nürnberg MR, Senn JW, Letzig D, Agnew SR. Acta Mater 2007;55:2101.
[6] Wassermann G, Grewen J. Texturen metallischer Werkstoffe. Berlin: Springer-Verlag; 1962.
[7] Kaiser F, Bohlen J, Letzig D, Kainer KU, Styczynski A, Hartig C. Adv Eng Mater 2003;5:891.
[8] Wendt J, Hantzsche K, Bohlen J, Kainer KU, Yi S, Letzig D. In: Kainer KU, editor. Magnesium. Weinheim: Wiley-VCH; 2009.
[9] Stanford N, Atwell D, Beer A, Davies C, Barnett MR. Scripta Mater 2008;59:772.
[10] Bohlen J, Yi S, Letzig D, Kainer KU. Mater Sci Eng 2010;A527:7092.
[11] Mishra RK, Gupta AK, Rao PR, Sachdev AK, Kumar AM, Luo AA. Scripta Mater 2008;59:562.

[12] Yi S, Brokmeier HG, Letzig D. J Alloys Compd 2010;506:364.
[13] Laser T, Hartig C, Nürnberg MR, Letzig D, Bormann R. Acta Mater 2008;56:2791.
[14] Lee JY, Lim HK, Kim DH, Kim WT, Kim DH. Mater Sci Eng A 2008;491:349.
[15] Humpreys FJ, Hatherly M. Recrystallization and related annealing phenomena. Oxford: Elsevier; 1996.
[16] Stanford N, Barnett MR. Mater Sci Eng A 2008;496:399.
[17] Barnett MR, Nave MD, Bettles CJ. Mater Sci Eng A 2004;386:205.
[18] Hantzsche K, Bohlen J, Wendt J, Kainer KU, Yi S, Letzig D. Scripta Mater 2010;63:725.
[19] Stanford N. Mater Sci Eng A 2010;527:2669.
[20] Couling SL, Pashak JF, Sturkey L. Trans ASM 1959;51:94.
[21] Sandlöbes S, Zaefferer S, Schestakow I, Yi S, Gonzales-Martinez R. Acta Mater 2011;59:429.
[22] Agnew SR, Yoo MH, Tome CN. Acta Mater 2001;49:4277.
[23] Agnew SR, Horton JA, Yoo MH. Metall Mater Trans A 2002;33(3):851.
[24] Chino Y, Kado M, Mabuchi M. Acta Mater 2008;56:387.
[25] Chino Y, Kado M, Mabuchi M. Mater Sci Eng A 2008;494:343.
[26] Ando S, Tonda H. Mater Sci Forum 2000;350–351:43.
[27] Koike J, Kobayashi T, Mukai T, Watanabe H, Suzuki M, Maruyama K, et al. Acta Mater 2003;51:2055.
[28] Yi S, Letzig D, Hantzsche K, Gonzalez-Martinez R, Bohlen J, Schestakow I, et al. Mater Sci Forum 2010;638–642:1506.
[29] Yasi JA, Hector Jr LG, Trinkle DR. Acta Mater 2010;58:5704.
[30] Fleischer RL. In: Peckner D, editor. The strength of metals; Reinold Press Edition, New York, 1964. p. 93.
[31] Fleischer RL. J Appl Phys 1962;33(12):3504.
[32] Chen K, Boyle KP. Metall Mater Trans A 2009;40:2751.
[33] Sandlöbes S, Friak M, Dick A, Zaefferer S, Yi S, Letzig D, et al. Acta Mater 2012;60:3011.
[34] Hohenberg P, Kohn W. Phys Rev B 1964;136:B864.
[35] Kohn W, Sham LJ. Phys Rev A 1965;140:A1133.
[36] Denteneer PJH, van Haeringen W. J Phys C: Solid State Phys 1987;20:L883.
[37] Vitos L, Nilsson J-O, Johansson B. Acta Mater 2006;54:3821.
[38] Dick A, Hickel T, Neugebauer J. Steel Res Int 2009;80:603.

[39] Kresse G, Hafner J. Phys Rev B 1993;47:558.
[40] Kresse G, Furthmuller J. Phys Rev B 1996;54:11169.
[41] Blöchl PE. Phys Rev B 1994;50:17953.
[42] Perdew JP, Burke K, Ernzerhof M. Phys Rev Lett 1996;77:3865.
[43] Pei Z, Zhu L-F, Friak M, Sandlöbes S, von Pezold J, Sheng HW, et al. New J Phys 2013;15:043020.
[44] Naumov AV. Russ J Non-Ferrous Met 2008;49:14.
[45] Bünzli J-CG. Acc Chem Res 2006;39:53.
[46] Yoo MH, Morris JR, Ho KM, Agnew SR. Metall Mater Trans A 2002;33:813.
[47] Reeh S, Music D, Gebhardt T, Kasprzak M, Jaepel T, Zaefferer S, et al. Acta Mater 2012;60:6025.
[48] Counts WA, Friák M, Raabe D, Neugebauer J. Acta Mater 2009;57:69.
[49] Raabe D, Sander B, Friák M, Ma D, Neugebauer J. Acta Mater 2007;55:4475.
[50] Steinmetz DR, Jäpel T, Wietbrock B, Eisenlohr P, Gutierrez-Urrutia I, Saeed-Akbari A, et al. Acta Mater 2013;61:494.
[51] Sandlöbes S, Friak M, Neugebauer J, Raabe D. Mater Sci Eng A 2013;576:61.
[52] Ai X, Quan G. Open Mater Sci J 2012;6:6.
[53] Mendis CL, Oh-ishi K, Kawamura Y, Honma T, Kamado S, Hono K. Acta Mater 2009;57:749.
[54] Meza García E. Suedwestdeutscher Verlag fuer Hochschulschriften (13 April 2011). ISBN-13: 978-383812478.
[55] Koike J, Kobayashi T, Mukai T, Watanabe H, Suzuki M, Maruyama K, et al. Acta Mater 2003;51:2055.
[56] Lee YC, Dahle AK, StJohn DH. Metall Mater Trans A 2000;31A:2895.
[57] Akhtar A, Teghtsoonian E. Acta Metall 1969;17:1339.
[58] Akhtar A, Teghtsoonian E. Acta Metall 1969;17:1351.
[59] Cáceres CH, Blake AH. Mater Sci Forum 2008;567–568:45.
[60] Cáceres CH, Blake AH. Phys Status Solidi (a) 2002;194:147.
[61] Blake AH, Cáceres CH. Mater Sci Eng A 2008;483–484:161.
[62] Yang YB, Wang FC, Tan CW, Wu YY, Cai HN. Trans Nonferrous Met Soc Ch 2008;18:1043.
[63] Agnew SR, Brown DW, Tome CN. Acta Mater 2006;54:4841.
[64] Fleischer RL. Acta Met 1962;10:835.